



1

THE MEASUREMENT OF FLOW-INDUCED SURFACE DISPLACEMENT ON A COMPLIANT SURFACE BY OPTICAL HOLOGRAPHIC INTERFEROMETRY

DTIC
ELECTE
FEB 02 1994
S
A

Tim Lee¹, Matt Fisher² W. H. Schwarz³
The Johns Hopkins University
Baltimore, Maryland 21218
U.S.A.

Abstract

Flow-induced surface displacements that form on a single-layer passive isotropic viscoelastic compliant surface as a result of the interaction with a turbulent boundary layer are measured by non-intrusive optical holographic interferometry in connection with an interactive fringe-processing system. Specific topographic features of a large section of the compliant surface are obtained in the form of interferometric fringe patterns. Information about the dimensions of the "foot prints" or the surface displacements of the turbulence on the compliant surface are presented in the form of line contours and isometric phase maps. These experimental data are essential in order to determine statistical measures of the random topography of the compliant surface. Furthermore, by coupling with the simultaneous measurements of the turbulence field, the physics of the alteration of the turbulent boundary layer by the undulating surface can then be better understood.

This document has been approved for public release and sale; its distribution is unlimited.

¹Postdoctoral Fellow, Department of Chemical Engineering

²Undergraduate Assistant, Department of Mechanical Engineering

³Professor, Department of Chemical Engineering

94-03238
9406



94 2 01 05 2
10

Nomenclature

A	Light amplitude
A_o	Light amplitude of object beam
A_r	Light amplitude of reference beam
c	Light speed
d_e	Diameter of laser beam
d_p	Diameter of pinhole
d_s	Spatial frequency
E	Exposure energy
f	Focal length
I_{in}	Light intensity at photographic plate
I_o	Light intensity of object beam
I_r	Light intensity of reference beam
k	wave number, $2\pi/\lambda$
L_{in}	Light amplitude records on the emulsion surface
L_o	Light ray of object beam
L_r	Light ray of reference beam
Re_x	Flow Reynolds number, $V_\infty x/\nu$
t	Time
t_e	Exposure time
T_o	Uniform background light transmittance
T_{re}	Reconstructed light through hologram
T_r	Amplitude transmittance of hologram
V_∞	Freestream flow speed
ω	Radian frequency, kc
x	Distance from the leading edge of the flat plate
z	Position
β	Slope
δ	Optical path difference
ϕ	Phase
ϕ_o	Phase of object beam
ϕ_r	Phase of reference beam
λ	Wavelength
θ_o	Angle between the object beam with respect to the normal of the photographic plate
θ_r	Angle between the reference beam with respect to the normal of the photographic plate
ν	Viscosity of water

Accession For	
NTIS	CRA&I <input checked="" type="checkbox"/>
DTIC	TAS <input type="checkbox"/>
Unannounced <input type="checkbox"/>	
Justification	
By	
Distribution /	
Availability Order	
Dist	Avail and/or Special
A-1	

ALL INFORMATION CONTAINED HEREIN IS UNCLASSIFIED

1. Introduction

The motion of a turbulent flow over a compliant surface causes a rich variety of fluid/surface interactions which have been actively studied for three decades (Landahl 1962, Hansen and Hunston 1974, Bushnell *et al.* 1977, Orszag 1979, Hansen *et al.* 1980, Gad-el-Hak *et al.* 1984, Duncan 1985 and 1986, Gad-el-Hak 1986, Riley *et al.* 1988, and others). The idea of using a compliant surface to alter a flow field was initially suggested by Kramer (1957) based on his observations of the swimming speeds of dolphins. The high water content and pliability of dolphin skin led to his belief that shear layer fluctuations may be damped, thereby leading to an extended region of the laminar boundary layer (delayed transition), and also affecting the turbulent boundary layer so as to produce significant drag reduction. However, later experimental and theoretical work has not provided a definite answer to the question how surface compliance affects drag and noise generation. Theoretical studies (Garrad and Carpenter 1982, Gaster 1985) indicate that transition of a laminar boundary layer to turbulence can be damped by a compliant surface. However, the interaction between a passive compliant surface and a turbulent boundary layer is still not well understood. Past investigations indicate that in order to provide a net reduction of skin-friction drag, it is necessary that the amplitude of the surface motions must be kept low enough to avoid causing a "roughness" effect which would increase, rather than decrease, the drag.

Conventional photographic methods have been employed extensively by investigators (Hansen and Hunston 1974, Hansen *et al.* 1980, Gad-el-Hak 1984, Gad-el-Hak 1986, Riley *et al.* 1988) to examine the compliant surface motion under a variety of flow conditions. Recently, direct vertical flow-induced surface-displacement measurements of a compliant surface beneath a

turbulent boundary layer have been carried out by Gad-el-Hak (1986) and Hess *et al.* (1991). Non-intrusive laser displacement detectors were developed to measure the instantaneous surface displacement at a chosen point. However, only one- or two-point measurements can be easily obtained by this technique. Information about the surface displacements on a large section of the compliant surface is needed in order to better understand the response of the compliant surface to the turbulence field. In the present experiment, the whole-field random topographic features of a compliant surface induced by a standard boundary layer in a water tunnel were acquired by non-intrusive optical holographic interferometry in connection with an interactive fringe-processing system.

The principle of optical holographic interferometry, also known as the wavefront reconstruction method, is based on the interference between light beams during exposure and diffraction during the reconstruction process. The pioneering work with recording and reconstruction of wavefronts was done by Gabor in 1948. Gabor's results stirred immediate interest, but it was not until the first off-axis laser hologram was made by Leith and Upatnieks (1963) that the technique became practically useful. In effect, one uses the holographic process to record a highly detailed three-dimensional image of the structure in its initial undeformed condition. When this shape is compared, by superposition, with the shape of the object in its deformed condition there results a pattern of interference fringes from which one can calculate, in terms of the wavelength of laser light, the extent of the surface displacement. The fringes in an interferogram are lines of constant optical path difference (OPD) between the wavefront under test and a reference wavefront. Adjacent fringes differ in OPD by a constant amount, usually one or one-half wavelength depending on the type of interferogram and the test set-up. Each

fringe is assigned an order number which represents the integral number of waves in phase between fringes.

One of the major applications of optical holographic interferometry is in the area of experimental mechanics deformation analysis, where highly sensitive and accurate holographic techniques are used to study small out-of-plane and in-plane displacements of the surface of the solid object (Archbold *et al.* 1967, Dudderar 1969, Ennos 1969, and others). In general, two basic variations of optical holographic interferometry are widely used, each possessing certain advantages over the other in particular test situations. Real-time or "live-fringe" holography consists of taking a single holographic exposure of an object in an unstressed or undeformed state, processing the photographic plate in place and reconstructing a hologram using the identical coherent reference beam to the one used in the construction process. The reconstructed image is now superimposed onto the original object, which is also illuminated with the same light as when the hologram was recorded. Interference fringes can now be seen if the object is displaced slightly. The interferometric comparison between the holographically reconstructed virtual image, i.e., the original undeformed state of the object, and the deformed state of the object is made at the instant it occurs. The particular advantage of the real-time method is that different types of motions, dynamic as well as static, can be studied with a single holographic exposure rather than having to make a hologram for each new position of the object. For double-exposure or "frozen-fringe" holography, the hologram plate is initially half-exposed with the object in an undeformed state and the exposure completed with the object in a deformed state. Upon reconstruction, the virtual image will be overlaid by a set of bright and dark interference fringes which are due to the displacement of the surface between the exposures.

Various techniques have been developed to interpret the surface deformations from the reconstructed holograms. An indirect multipoint-observation method has been proposed for determining the displacement field of an object from its usual double-exposure hologram (Haines and Hildebrand 1966, Ennos 1969, Sollid 1969, Dhir and Sikora 1972, and Pryputniewicz and Bowley 1978). However, due to the large amount of work involved, this technique is, in general, time consuming and is limited to small numbers of holograms.

Direct-readout holographic techniques, utilizing heterodyne and phase-shifting interferometry, are usually employed when large numbers of holograms are required. The first direct-readout holographic technique developed was electronic speckle pattern interferometry which measures surface deformations and contours at video rate (e.g., Butters and Leenderz 1971, Nakadate *et al.* 1983). In this technique, a speckle pattern exposure is taken of the object in one position. Then the object is deformed, and another exposure is taken. These two speckle patterns are subtracted, and their difference is squared to obtain speckle correlation fringes corresponding to the object's deformation. Electronic speckle pattern interferometry has been useful for qualitative measurements but has some difficulties in producing good quantitative results since it is hard to determine the fringe centers.

Accurate phase measurements (i.e., of deformations) can be acquired using digital holographic interferometry (DHI) by combining double-exposure holography and the phase-shifting interferometry technique (e.g., Hariharan 1982, Breuckmann and Thieme 1985, and others). The interference phase at each point is obtained from the intensities, which is determined for at least three different phase relationships of the reference wave at each point without analyzing the surrounding points. The phase at each point is calculated from the

intensities of the secondary fringes recorded at different relative phase shifts. DHI requires the making of an intermediate hologram with the object in place. The accuracy of DHI is of the order of $\lambda / 100$ (λ is the wavelength of the laser light).

In order to overcome the needs for an intermediate recording step, and the chemical processing, an in-line image holographic technique called digital speckle pattern interferometry (DSPI) was proposed by Creath (1985). In DSPI, the phase is calculated directly and there is no need to process the speckle data to form speckle correlation fringes and locate fringe centers (as required in the electronic speckle interferometric method). However, when the phase-shifting interferometric techniques are applied to speckle interferometry, the randomness of the speckles usually causes noisy data. The accuracy of DSPI is of the order of $\lambda / 10$.

All the holographic techniques discussed above are subject to one or several of the following disadvantages: (1) double-exposure hologram; (2) undesirable hologram quality and accuracy; (3) the phase measurements can only be obtained at the video frame rate; (4) limited to small numbers of holograms; and (5) the surface deformations cannot vary instantaneously and continuously as a function of time. However, in order to better understand the interaction between the motion of a compliant surface and the near-wall turbulence field, it is important to be able to monitor the evolution of the flow-induced surface displacement of the compliant surface as a function of time, therefore, a real-time optical holographic interferometry was adopted in the present experiment.

2. Theoretical Background

2.1. Wavefront recording

In holography, a laser light ray (L) moving in the positive z-direction (i.e., approaching the photographic plate) with a velocity c may be expressed in the form (Coolier, *et al.* 1971):

$$L = A \cos[k(z - ct + \delta)] = A \cos(kz - \omega t + \phi) \quad (1)$$

where A is the amplitude, $k (= 2\pi/\lambda)$ is the wave number, t is the time, δ is the optical path difference and is related to the phase, $\omega (= kc)$ is the angular frequency of the light, and $\phi (= k\delta)$ is the phase in radians. Constructive and destructive interference are obtained by adding two wave trains depending upon their relative phases. However, real objects may be considered as a collection of many points each of which reflects outwardly spherical waves. Light from nearby points interacts by constructive and destructive interference to form very complicated wavefronts unique to the particular object. Furthermore, for two monochromatic light waves (e.g., the reference and the object waves, L_r and L_o) that travel through same medium and are simultaneously incident on a plane ($z = 0$), we may write

$$L = Ae^{i\phi} \quad (2)$$

Typical schemes for recording the light reflected from the compliant surface is shown in figure 2 in section 3.3. below. The laser light is divided by a beam splitter (BS1) so that part of the light follows a path which is called the reference beam (solid line) and the rest of the light illuminates the object. Wavefronts reflected from the object form the illumination beam (dashed line). After exposure and subsequent developing, the plate is called a hologram. The whole of the information is recorded and stored on the plate, but in highly coded form. The hologram

itself may be regarded as a complicated diffraction grating with variable pitch and variable orientation. There is no similarity between the appearance of the hologram and the object used to form it. The information can be decoded or the image of the object can be reconstructed by illuminating the hologram with the reference beam.

2.2. Interference-fringe pattern formation

The light used to illuminate the object must be temporally and spatially coherent. A beam of coherent monochromatic light illuminates the object, and the light reflected from it falls on the photosensitive surface (i.e., the emulsion) of the photographic plate. The light amplitude, L_{in} , that is recorded on the emulsion surface is

$$L_{in} = L_r + L_o = A_r e^{i\phi_r} + A_o e^{i\phi_o} \quad (3)$$

where L_r (L_o), A_r (A_o) and ϕ_r (ϕ_o) represent the light ray, the amplitude and the phase of the reference (object) beam, respectively. The intensity, I_{in} , at the photographic plate when the hologram is recorded as

$$I_{in} = L_{in} L_{in}^* = A_r^2 + A_o^2 + A_r A_o [e^{i(\phi_o - \phi_r)} + e^{-i(\phi_o - \phi_r)}] \quad (4)$$

or

$$I_{in} = I_r + I_o + 2(I_r I_o)^{1/2} \cos(\phi_o - \phi_r) \quad (5)$$

Equation (5) reveals that the intensity is modulated by the cosine of the difference in phases of the two incident waves at each point, resulting in an interference-fringe pattern.

2.3. Wavefront reconstruction

By assuming that the amplitude transmittance of the photographic plate after processing is linearly related to the exposure energy (E), the transmittance amplitude (T_r) of the hologram

is

$$T_t = T_0 + \beta t_e I_{in} \quad (6)$$

where T_0 is the uniform background light transmittance, β is slope (negative) of T , versus E that is characteristic of the emulsion of that specific photographic plate; and t_e is the exposure time.

Therefore, when the hologram is reconstructed (i.e., illuminated by the same reference beam, $A_r \exp(i\phi_r)$), the light transmitted from the hologram is

$$T_{re} = A_r e^{i\phi_r} [T_0 + \beta t_e (A_r^2 + A_0^2) e^{-i(\phi_r - 2\phi_0)} + \beta t_e A_r^2 A_0 e^{i\phi_0}] \quad (7)$$

Equation (7) indicates that the original object light wave $L_0 (=A_0 \exp(i\phi_0))$ has been regenerated by diffraction from the hologram. It is identified as the last term in equation (7) and is called the virtual-image beam (except with a constant factor $\beta t_e A_r^2$). This image reconstruction is shown in figure 1 as the first-order diverging diffracted beam. The second term in equation (7) also contains object phase information (ϕ_0) and is called the conjugate-image beam (shown as the first-order converging diffracted beam in figure 1). The first term does not contain ϕ_0 and is called the undiffracted beam or directly transmitted beam (shown as the zero-order undiffracted beam in figure 1).

The reconstructed image is identical in appearance to the real object and is used as the reference against which to compare the wavefront reflected by the deformed object. Interference fringes are formed when the wavefront reflected from the deformed object interacts with that generated by the hologram; these fringes indicate the deviation of the deformed object from the undeformed object as reconstructed by the hologram.

3. Experimental Method and Fringes Analysis

3.1. *Description of Flow Facility*

The closed-loop, low-turbulence, stainless-steel water tunnel at the National Institute of Science and Technology was used in the present experiments. The test section is 0.6 m in diameter and 3 m in length. To generate a turbulent boundary layer, a stainless steel flat plate (4 m long and 0.6 m wide) is rigidly mounted within the test section along the centerline of the test section. The 4.8 cm thick flat-plate assembly consists of a 6.3 mm highly polished top cover on which a fully-developed turbulent boundary layer is generated. A flap was mounted on the downstream end of the plate to control the pressure distribution about the plate as well as the angle of attack at the leading edge. Reynolds numbers ($Re_x = V_\infty x/\nu$, where V_∞ is the free stream velocity, x is the distance from the leading edge of the plate, and ν is the kinematic viscosity of the fluid) of: 5.2×10^5 , 9.4×10^5 , 1.04×10^6 , and 1.43×10^6 were investigated.

3.2. *Compliant Material Formation and Characteristics*

A single-layer isotropic viscoelastic compliant surface was used in the present experiment. The compliant materials were made by mixing commercially available RTV silicone elastomer (Dow-Corning Sylgard 184) and silicone oil (Dow-Corning 200 series Silicone oil). The mixtures were chosen in accordance with Duncan's (1985, 1986) theoretical results to produce small amplitude, stable displacements on the compliant surface which represent the footprint of an individual flow structure in the shear layer. The amount and viscosity of the oil in the mixture can be varied to change the viscoelastic properties of the compliant material and allows one to alter the response of the compliant surface to the flow Reynolds numbers of interest. The compliant surfaces were prepared in 3.8 cm deep plexiglass trays which were placed flush in the

flat plate and which cover about 10 percent of the working surface. A compliant mixture with 91 percent by weight of 100 cSt oil and 9 percent of elastomer was used in our experiment. White, silicone-based colorant (Ferro Corp.), approximately 4.5 percent by weight, was added to the mixture to render the original transparent material opaque for the purposes of scattering incident laser light. The low-frequency shear modulus of this compliant mixture was measured with a Weissenberg rheogoniometer at the Johns Hopkins University, and found to be 2300 dynes/cm² [Hess, 1990].

3.3. *Optical Arrangement for Optical Holographic Interferometry*

Off-axis reference-beam and transmission holographic interferometry was used in the present experiment. The optical arrangement is illustrated in figure 2. A 20-watt argon laser (Spectra Physics Model 2030) yielding 8.8 watt of power at a wavelength of 514 nm was used as the coherent light source in construction of the holograms and reconstruction of their images. Generally, since the object are not highly reflecting, most of the object light doesn't reach the hologram due to absorption and scattering losses at the object. In order to maximize the amount of light reaching the surface of the compliant surface, a beam splitter (BS1), with a transmission and reflectivity of 70 and 30 percent, respectively, was used. The illumination beam (dashed line) was expanded by a short-focal-length microscope objective lens (EL1). A collimating lens (CL) was used to maintain the intensity of the expanded illumination beam as well as to vary the illuminated area of the compliant surface of interest.

Mirrors (M1, M2 and M3) were used to compensate the optical-path-length difference between the illumination-object beam and the reference beam. When light from a given source is divided by a beam splitter (e.g., BS1) so as to travel by two different paths, it only forms

interference fringes when reunited if the difference between the two path lengths is less than the coherence length of the laser (which is of about 5 cm in the present experiment).

A beam splitter (BS2) and neutral density filters (NDF) were used to obtain a large enough beam ratio (the relative intensities of the reference and object beams) to keep the unwanted intermodulation noise (which are the interference fringes that result from the scattered light rays interfere with each other) low, and to conserve a linear response of the photographic emulsion to the exposure energy. Also, the beam ratio needs to be kept low, since too great a ratio between the intensities of the reference and object beams is undesirable and could result in a hologram with too little contrast between the maxima and the minima in the recorded surfaces. In fact a ratio of 1:1 would be desirable if the intermodulation noise were not a consideration. A hologram recorded with a beam ratio of 3.2:1 was found to have the best diffraction efficiency and contrast in the present experiments.

A microscope objective lens (EL2) was used to expand the reference beam illuminating the photographic plate. In order to keep the signal-to-noise ratio at a reasonable level, the expanded beams have to be free of spatial noise. A pinhole (PH) filter placed at the focal point of the lens is used to obtain a uniform, spatial noise-free illumination. The pinhole size, $d_p (= 2d_f)$ was chosen to be about two times of the beam focusing diameter, $d_f (= 4\lambda f/\pi d_o$, f is the focal length of the optics and d_o is the diameter of laser beam). Due to the high laser power of the illuminating beam (about 6.2 watts), no pinhole filter or spatial filter was installed within the illumination-object-beam path.

Since the illumination-object beam passes through the water-air medium which causes a change of about 33 percent in the light speed variation, a tube of water was placed in the

reference beam path so as to compensate the optical path-length difference between the reference beam and the illumination-object beam and to ensure that the interference between two wave trains was observable; and their relative phases ($\phi_o - \phi_s$) were fairly constant with time. This can be demonstrated from equation (1) which indicates that ω is of the order of 10^{15} which is much too fast to be observed visually or with any optical instrument. The length of the tube of water was kept the same as the illumination-object-beam path length through the water tunnel. A photograph of the optical experimental set-up is shown in figure 3.

A specially built liquid-gate was used to develop and process the photographic plate *in situ* to eliminate problem of relocation of the plate in real-time holography. Also, by exposing and viewing the holograms in distilled water, changes in emulsion thickness (i.e., local deformations of the emulsion due to non-uniform drying) were reduced to an acceptable level (Hariharan and Ramprasad 1973). The plates were Agfa-Gevaert 10E56HD; and the exposure time was one millisecond. The holograms were developed in Kodak D-19 for approximately 4 min and then fixed in the normal manner. The chemical solutions were introduced into the liquid-gate by a simple gravity system.

In order to avoid any small motions of the recording material and the optical components during the exposure which could result in a marked loss of diffraction efficiency, or even dark bands across the hologram, the stability of the system was checked using Michelson interferometry. The same set-up was employed to determine the coherence length of the laser used in the present experiment. The spatial frequency or angular aperture (i.e., $1/d_s$, where d_s is the space or pitch between the interference fringes on the hologram), given by

$$d_s = \lambda / (\sin \theta_o + \sin \theta_s) \quad (8)$$

where θ_o and θ_r are the angles between the object beam and the reference beam with respect the normal of the photographic plate, was kept smaller than the maximum resolution of the emulsion of the photographic plate to obtain a good hologram.

The reconstructed interferometric fringes or interferograms were routed to an image digitizer (DT 2861) via a CCD camera (Pulnix TM-840) to produce 512x480 image elements with 256 gray levels and stored in a frame buffer for phase (i.e., of surface displacement) determination.

3.4. Interpretation of Fringe Patterns

Fringe identification and ordering were performed using a combination of menu/mouse driven fringe processing packages named FAST (1987) from a graphics tablet. FAST is also an advanced graphics package which allows interactive screen displays of three-dimensional phase plots, X, Y and radial profiles, and contour plots running on a IBM PC microcomputer. In FAST, an interferogram representing the optical path difference is placed on the graphics tablet and analyzed by digitizing the fringe-order-center using the cross-hair four button cursor to enter the fringe coordinates. The results are presented in both numeric and graphics displays. This interactive fringe-processing technique is similar to the keyboard-driven cursor system used by Seguchi *et al.* (1979) and Funnell (1981). The resolution of the graphics digitizing tablet is typically 25 microns. The phase (i.e., of surface displacement) accuracy achieved by this technique is of the order of $\lambda/30$. The amount of deformation is then obtained from the interferometric fringe pattern, if the wavelength and the order number N of the fringe is known, by applying the relation $\delta = N\lambda$.

The capabilities of FAST for analyzing the interferometric fringe pattern can be summarized as follows: (1) automatic and self-ordering of any combination of open and closed fringe patterns,

regardless of shape and orientation; (2) fringe center positions are determined to fractional pixel values; (3) results are shown in the forms of a line-contour, isometric phase map, and X-Y profile plots; (4) wide range of acceptable fringe contrast and density; and (5) smoothing functions are included to reduce the effects of spatial noise on the interferometric fringe pattern.

4. Results

Several double-exposed holograms were recorded at different Re_x and then reconstructed using the optical set-up shown in figure 2. The photographic plates were initially exposed at a static state, which gives the reference or comparison surface, and then followed by a second exposure at a specified flow speed. The exposure time was fixed at one millisecond. The dimension of the reconstructed fringe pattern is 5 cm in diameter for the photographs shown below, and the flow direction is from left to right.

Figure 4 is a photograph of the reconstructed interferometric fringes on a compliant surface from a double-exposed hologram at $Re_x = 5.2 \times 10^5$. A hot-film probe shown on the left side of this photograph was used as a reference length; the distance between the two prongs is 3 mm. Figures 5a and 5b show the corresponding line contours and the isometric phase map that were analyzed using the FAST interactive fringe-processing system. Due to the quality of the photograph (Fig. 4), more fringe centerlines were traced and shown as line contours of the phase map (Fig. 5a). The peak-to-valley surface displacement is 1.67 μm and the *rms* value is 0.32 μm . Typical X-Y profiles, i.e., the variations of the amplitude of the surface displacement, through the center of the interferogram, along the X- and Y- direction are shown in figures 6a and 6b. For example, the surface displacement at the center of the interferogram (figure 6) was found to

have a magnitude of 0.48 μm . The X-Y profiles also demonstrate that statistical information at or between any point on the surface displacement can be acquired from the interferogram using a real-time holographic method.

When interpreting live- or frozen-fringe patterns, it is important to remember that the interferometric fringes corresponding to $N = 0, 1, 2, \dots$ are bright fringes in the reconstruction from a double-exposure frozen-fringe pattern, whereas the dark fringes result from the live-fringe case. This follows from the fact that frozen fringes result from the interference between two nearly similar reconstructed waves from a single hologram plate, while the live fringes result from interference between the reconstructed wave and the wave directly from the object.

Figure 7 shows the photograph of the reconstructed interferometric fringes with a second exposure at $Re_x = 9.4 \times 10^5$. More complicated and closed-ring fringes are seen 7 as compared to figure 4, which indicates that the magnitude of the compliant-surface deformations, induced by the random forcing of the turbulence field, increases with Reynolds numbers. Similar phenomena are also demonstrated in figures 11 and 13 shown below. The corresponding complete set of interferometric fringes of figure 7 traced by the interactive software with a microcomputer is shown in figure 8. Figures 9a and 9b show the line contours and the isometric phase map of figure 7 with a peak-to-valley amplitude of 2.93 μm and a *rms* value of 0.58 μm . The corresponding X-Y profiles, through the center of the interferogram, are shown in figures 10a and 10b which give the variations of the surface displacement along the X and Y directions.

Figure 11 shows the photograph of the reconstructed double-exposed interferometric fringes at $Re_x = 1.04 \times 10^6$. The corresponding isometric phase map and the Y-profile are shown in figures 12a and 12b. The peak-to-valley and the *rms* magnitude of the compliant-surface

displacements at this Re_x were found to be 3.82 μm and 0.72 μm , respectively.

Figure 12 is the photograph of the reconstructed interferometric fringes at $Re_x = 1.43 \times 10^6$. By comparing the density of the interferometric fringes and the number of the closed-ring fringes to the other photographs (e.g., figures 4, 7, and 11), it is found that the fringes become dense and widely distributed in space and are difficult to view accurately or to photograph for this particular compliant surface. One needs to focus on a smaller illuminated area of the compliant surface so as to accurately trace the interferometric fringes accurately for higher Re_x .

5. Summary

A non-intrusive method employing optical holographic interferometry in connection with an interactive fringe-processing system was utilized to determine the small flow-induced surface displacements (less than 50λ) of a compliant surface beneath a turbulent boundary layer. This technique is particularly useful for determining the time-evolution and instantaneous surface displacements of a large portion of a compliant surface. Statistical information (e.g., such as displacement probability density functions, space-time correlations, displacement-velocity cross-correlations, displacement-velocity joint probability density functions) at or between any point on the surface displacements in conjunction with simultaneous velocity field measurements can be obtained. This information is important in order to understand the nature of the stable pattern of the compliant-surface displacements and also how the stable response of the compliant surface alters the near-wall turbulent flow structure. Finally, although the double-exposure hologram was used to verify the optical and fringe-processing systems, there seems no reason why equally good results should not be achieved using the same optical system for real-time holography.

Acknowledgements

This work was supported by the Office of Naval Research under contract N00014-87-K-0126. The kind assistance of D.E. Hess and G.E. Mattingly in the National Institute of Science and Technology is greatly appreciated. The assistance of D. Basila and C. Koliopoulos of the Phase Shift Technology is also acknowledged.

References

- Archbold, E.; Burch, J.M.; Ennos, A.E. 1967: The application of holography to the comparison of cylinder bores. *Journal of Physics E.: Scientific Instruments*, 44, pp.489-494.
- Breuckmann, B.; Thieme, W. 1985: Computer-aided analysis of holographic interferograms using the phase-shift method. *Applied Optics*, 24, pp.2145-2150.
- Bushnell, D.M.; Hefner, J.N. 1977: Effect of compliant wall motion on turbulent boundary layers. *Physics of Fluids*, 20, pp.S31-S48.
- Butters, J.N.; Leenderz, J.A. 1971: Speckle pattern and holographic techniques in engineering metrology. *Optics and Laser Technology*, 3, pp.26.
- Coolier, R.J.; Burckhardt, C.B.; Lin, L.H. 1971: Optical Holography. Academic Press, Inc., San Diego, California.
- Creath, K.; 1985: Phase-shifting speckle interferometry. *Applied Optics*, 24, pp.3053-3058.
- Dhir, S.K.; Sikora, J.P. 1972: An improved method for obtaining the general-displacement field from a holographic interferogram. *Experimental Mechanics*, 12, pp.323-327.
- Dudderar, T.D.; 1969: Applications of holography to fracture mechanics. *Experimental Mechanics*, 9, pp.281-285.
- Duncan, J.H.; Waxman, A.M.; Tulin, M.P.; 1985: The dynamics of waves at the interface between a viscoelastic coating and a fluid flow. *Journal of Fluid mechanics*, 158, pp.177-197.
- Duncan, J.H.; 1986: The response of an incompressible, viscoelastic coating to pressure fluctuations in a turbulent boundary layer. *Journal of Fluid Mechanics*, 171, pp.339-363.
- Ennos, A.E.; 1968: Measurement of in-plane surface strain by hologram interferometry. *Journal of Physics E:Scientific Instruments*, 1, pp.731-734.
- FAST; 1987: Phase Shift Technology, 1430 East Fort Lowell, Tucson, AZ 85719.
- Funnel, W.R.J.; 1981: Image processing applied to the interactive analysis of interferometric fringes. *Applied Optics*, 20, pp.3245-3250.
- Gabor, D.; 1948: A new microscope principle. *Nature*, 161, pp.777-778.

- Gad-el-Hak, M.; Blackwelder, R.F.; Rilley, J.J.; 1984: On the interaction of compliant coating with boundary-layer flows. *Journal of Fluid Mechanics*, 140, pp.257-280.
- Gad-el-Hak, M.; 1986: The response of elastic and viscoelastic surfaces to a turbulent boundary layer. *Journal of Applied Mechanics*, 53, pp.206-212.
- Garrad, A.D.; Carpenter, P.W.; 1982: A theoretical investigation of flow induced instabilities in compliant coating. *Journal of Sound and Vibration*, 85, pp.483-500.
- Gaster, M.; 1985: Growth of instability waves over compliant coating. *Bull. Amer. Phys. Soc.*, 30, p.1708.
- Haines, K.A.; Hildebrand, B.P.; 1966: Surface-deformation measurement using the wavefront reconstruction method. *Applied Optics*, 5, pp.595-602.
- Hansen, R.J.; Hunston, D.L.; 1974: An experimental study of turbulent flows over compliant surfaces. *Journal of Sound and Vibration*, 34, pp.297-308.
- Hansen, R.J.; Hunston, D.L.; Ni, C.C.; Reischman, M.M.; 1980: An experimental study of flow-generated waves on a flexible surface. *Journal of Sound and Vibration*, 68, pp.317-334.
- Hariharan, P.; Ramprasad, B.S.; 1973: Rapid *in situ* processing for real-time holographic interferometry. *Journal of Physics E.: Scientific Instruments*, 6, pp.699-701.
- Hariharan, P.; Oreb, B.F.; Brown, N.; 1982: A digital phase-measurement system for real-time holographic interferometry. *Optics Communication*, 41, pp.393-396.
- Hess, D.E.; 1990: An experimental investigation of a compliant surface beneath a turbulent boundary layer. Ph.D. dissertation, Johns Hopkins University, Baltimore, Maryland
- Hess, D.E.; Peattie, R. A.; Schwarz, W.H.; 1991: A non-intrusive method for the measurement of flow-induced surface displacement of a compliant surface. *Experiments in Fluids* (paper in review).
- Kramer, M.O.; 1957: Boundary layer stabilization by distributed damping. *Journal of the Aeronautical Sciences*, 41, pp.259-281.
- Landahl, M.T.; 1962: On the stability of a laminar incompressible boundary layer over a flexible surface. *Journal of Fluid Mechanics*, 13, pp.609-632.
- Lanzel, F.; Schluter, M.; 1977: Video-electronic analysis of holographic interferograms. *Proceeding of Society of Photo-Optic Instrument Engineering*, 136, pp.166.

Leith, E.N.; Upatnieks, J.; 1963: Wavefront reconstruction with continuous-tone objects. *Journal of Optical Society of America*, 53, pp.1377.

Nakadate, S.; Yatagal, T.; Saito, H.; 1983: Computer-aided speckle pattern interferometry. *Applied Optics*, 22, pp.237-243.

Orszag, S.A.; 1979: Prediction of compliant wall drag reduction. NASA Contract report 3071.

Pryputniewicz, R.J.; Bowley, W.W.; 1978: Techniques of holographic displacement measurement: an experimental comparison. *Applied Optics*, 17, pp.1748-1756.

Riley, J.J.; Gal-el-Hak, M.; Metcalf, R.W.; 1988: Compliant coating. *Annual Review of Fluid Mechanics*, 20, pp.393-420.

Seguchi, Y.; Tomita, Y.; Watanabe, M.; 1979: Computer-aided fringe-pattern analyzer - a case of photoelastic fringe. *Experimental Mechanics*, 19, pp.362-370.

Sollid, J.E.; 1969: Holographic interferometry applied to measurements of small static displacements of diffusively reflecting surfaces. *Applied Optics*, 8, pp.1587-1595.

Figure Captions

- Figure 1. The geometry for hologram image reconstruction.
- Figure 2. Schematic representation of the experimental set-up for optical holographic interferometry: BD, beam dump; BS, beam steerer; BS1, BS2, beam splitters; BS3, BS4, beam stops; CL, collimating lens; EL1, EL2, expanding lenses; LGPH, liquid-gate and plate holder; M1, M2, M3, M4, M5, mirrors; PH, pinhole; PP, photographic plate; S, shutter; WT, water tube.
- Figure 3. Photograph of the experimental set-up.
- Figure 4. Photograph of the reconstructed interferometric fringes or interferogram at $Re_x = 5.2 \times 10^5$.
- Figure 5. Line contours and isometric phase map of the interferogram shown in figure 4: (a) line contours, and (b) isometric phase map.
- Figure 6. Typical X-Y profile of the interferogram shown in figure 4: (a) X-profile, and (b) Y-profile.
- Figure 7. Photographs of the reconstructed interferometric fringes at $Re_x = 9.4 \times 10^5$.
- Figure 8. Fringe tracing or the digitized fringe data of the interferogram shown in figure 7.
- Figure 9. Line contours and isometric phase map of the interferogram shown in figure 7: (a) line contours, and (b) isometric phase map.
- Figure 10. Typical X-Y profile of the interferogram shown in figure 7: (a) X-profile, and (b) Y-profile.
- Figure 11. Photographs of the reconstructed interferometric fringes at $Re_x = 1.04 \times 10^6$.
- Figure 12. Isometric phase map and the Y-profile of the interferogram shown in figure 11: (a) isometric phase map, and (b) Y-profile.
- Figure 13. Photographs of the reconstructed interferometric fringes at $Re_x = 1.43 \times 10^6$.

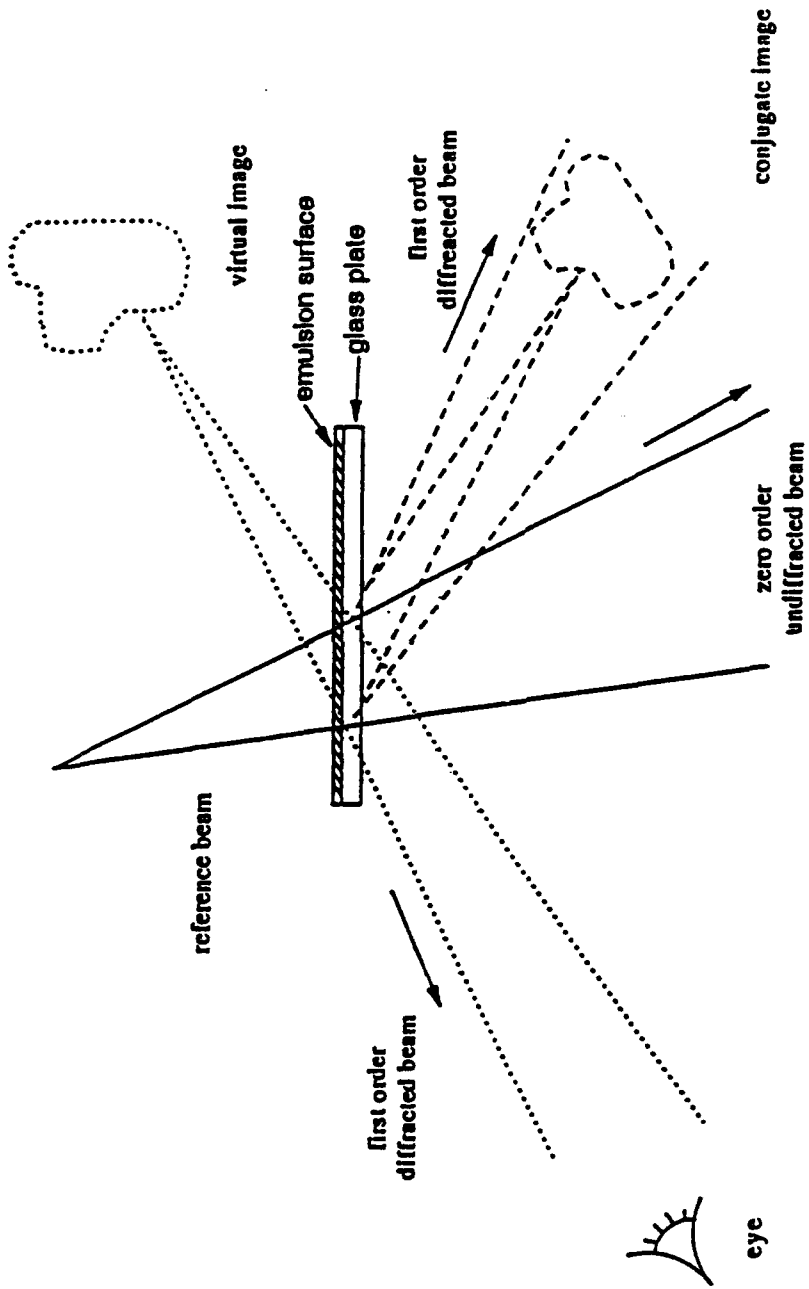


Figure 1. The geometry for hologram image reconstruction.

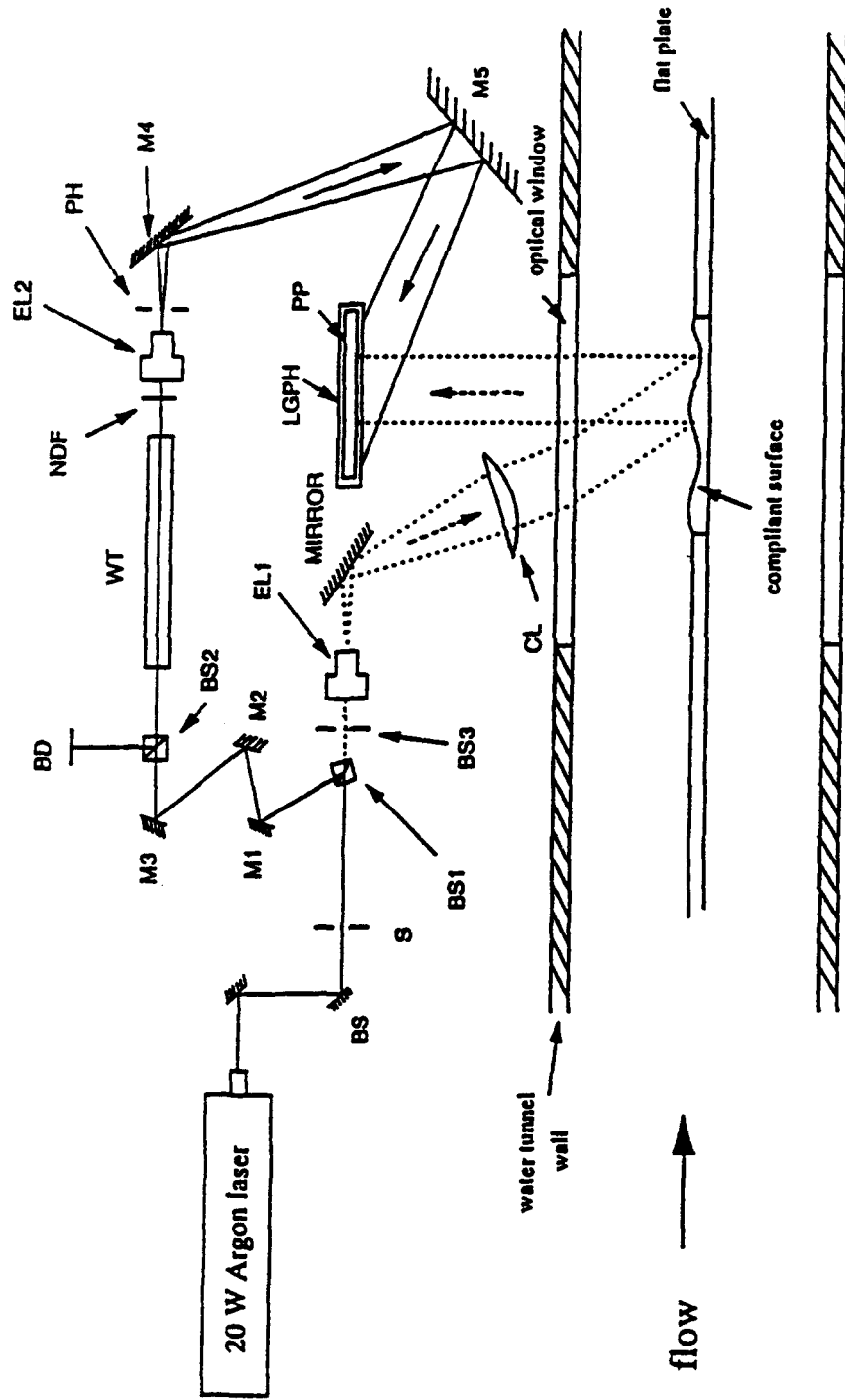


Figure 2.

Schematic representation of the experimental set-up for optical holographic interferometry; BD, beam dump; BS, beam steerer; BS1, BS2, beam splitters; BS3, BS4, beam stops; CL, collimating lens; EL1, EL2, expanding lenses; LGPH, liquid-gate and plate holder; M1, M2, M3, M4, M5, mirrors; PH, pinhole; PP, photographic plate; S, shutter; WT, water tube.

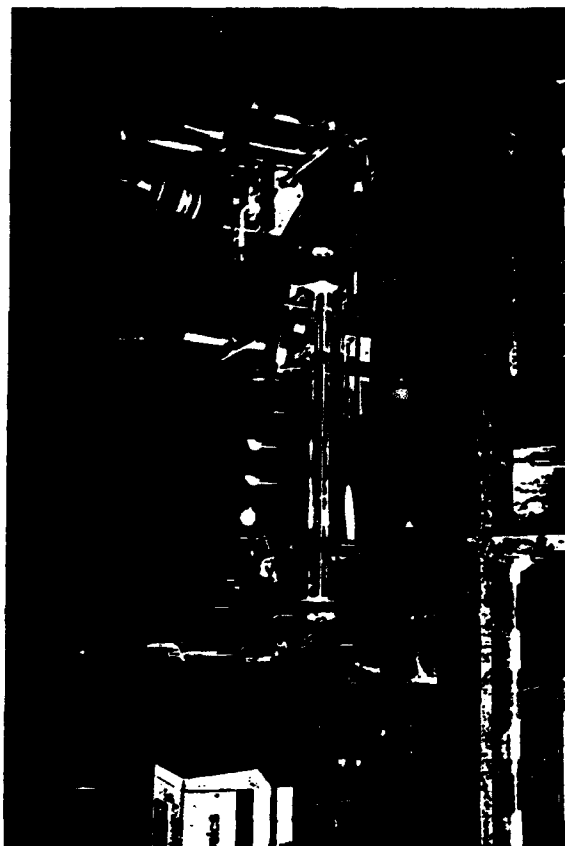


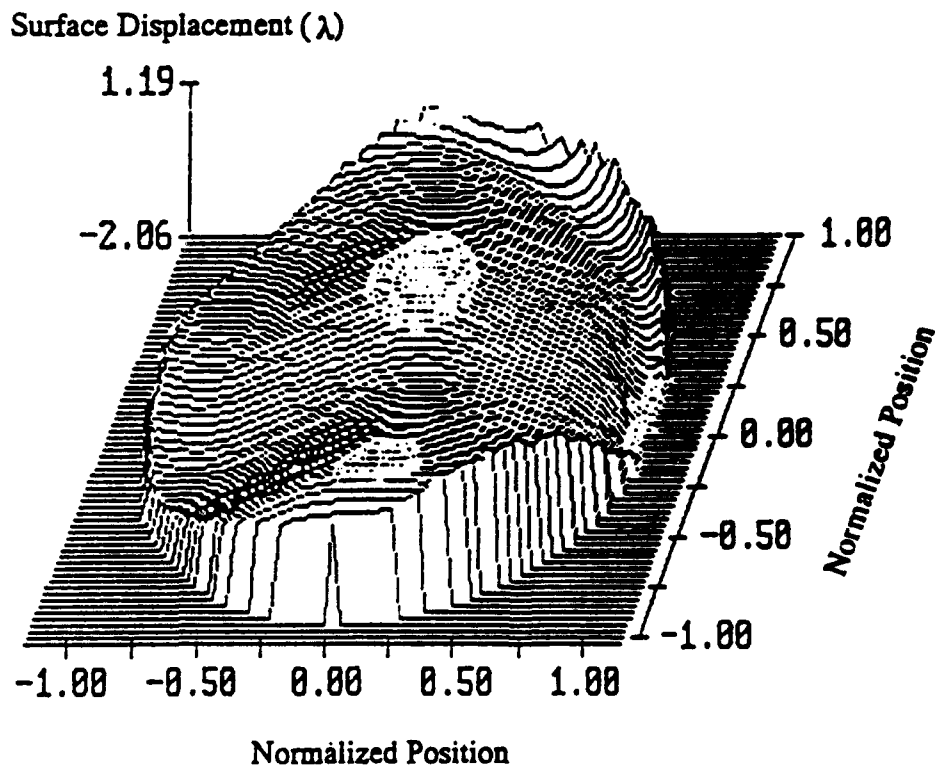
Figure 3. Photograph of the experimental set-up.



Figure 4. Photograph of the reconstructed interferometric fringes or interferogram at $Re_x = 5.2 \times 10^5$.



(a)



(b)

Figure 5. Line contours and isometric phase map of the interferogram shown in figure 4: (a) line contours, and (b) isometric phase map.

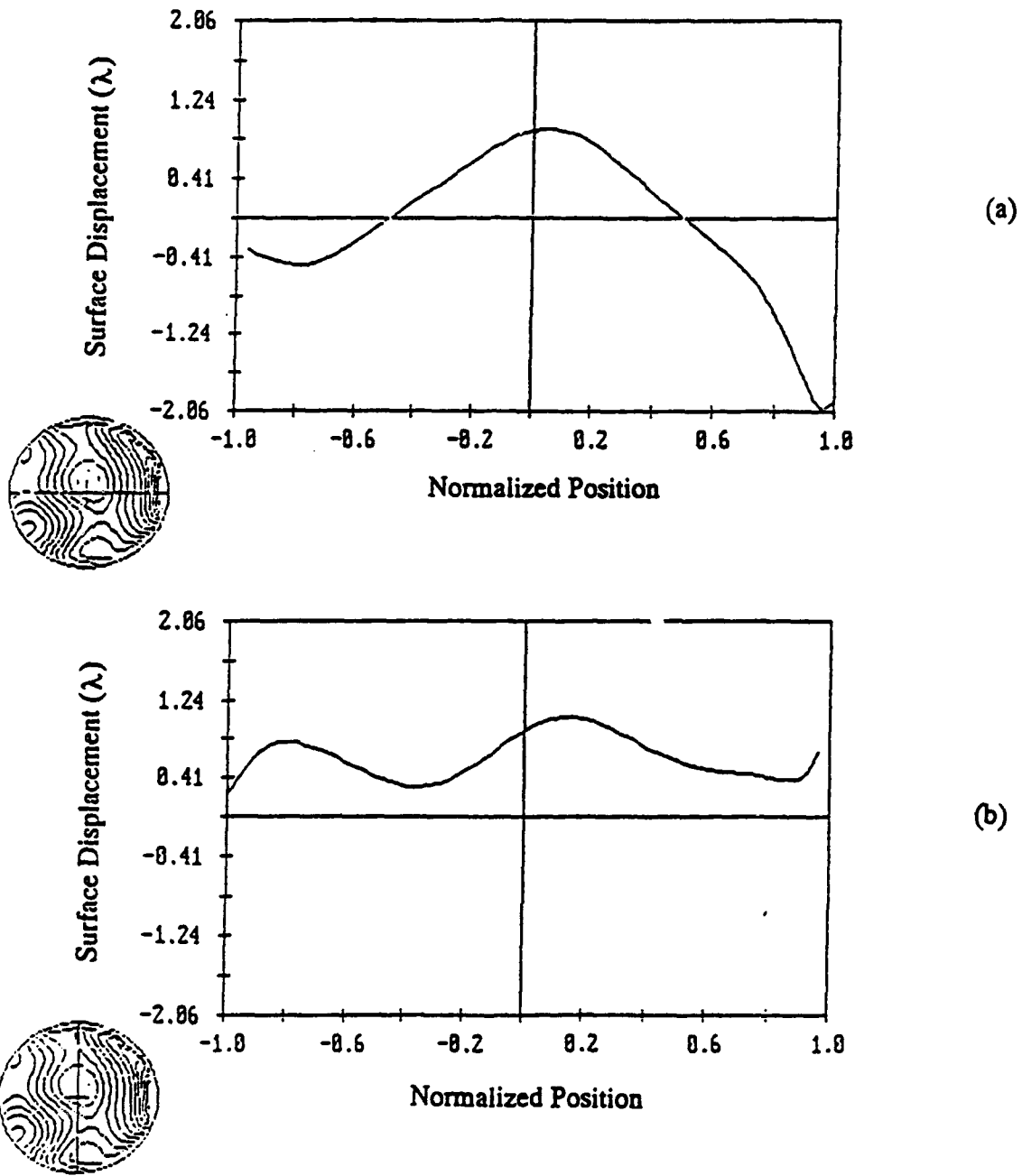


Figure 6. Typical X-Y profile of the interferogram shown in figure 4: (a) X-profile, and (b) Y-profile.



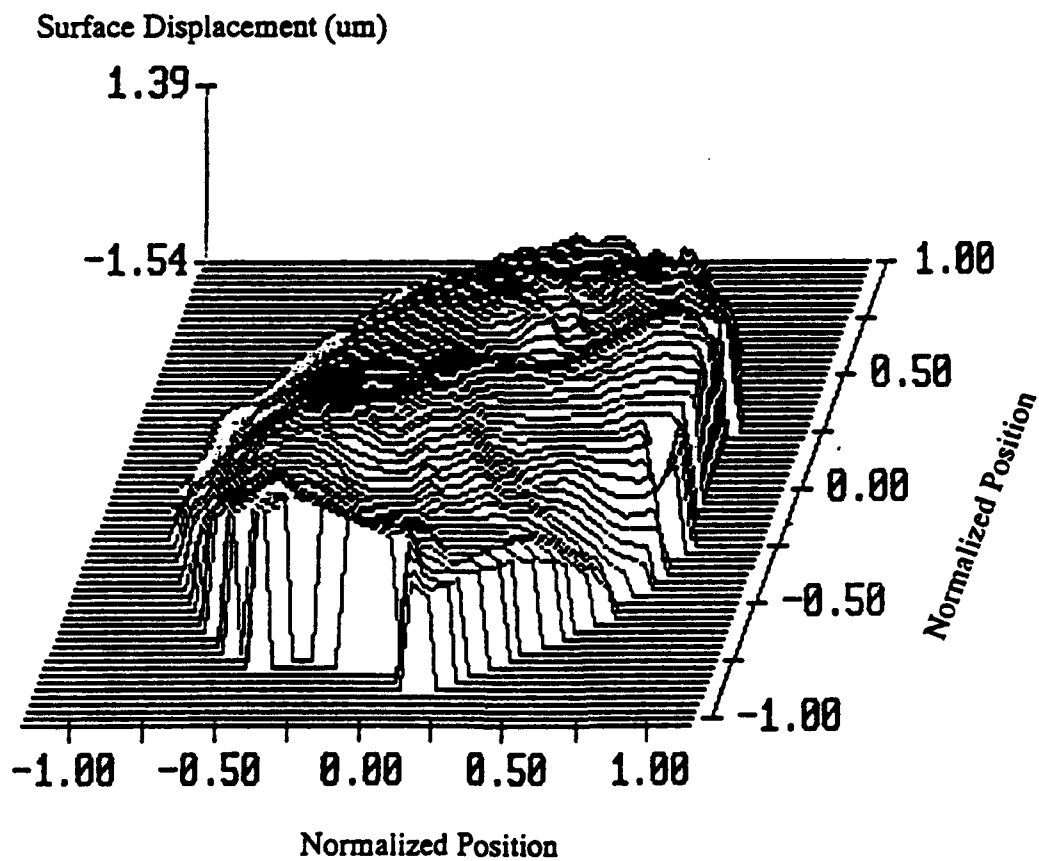
Figure 7. Photographs of the reconstructed interferometric fringes at $Re_x = 9.4 \times 10^5$.



Figure 8. Fringe tracing or the digitized fringe data of the interferogram shown in figure 7.



(a)



(b)

Figure 9.

Line contours and isometric phase map of the interferogram shown in figure 7: (a) line contours, and (b) isometric phase map.

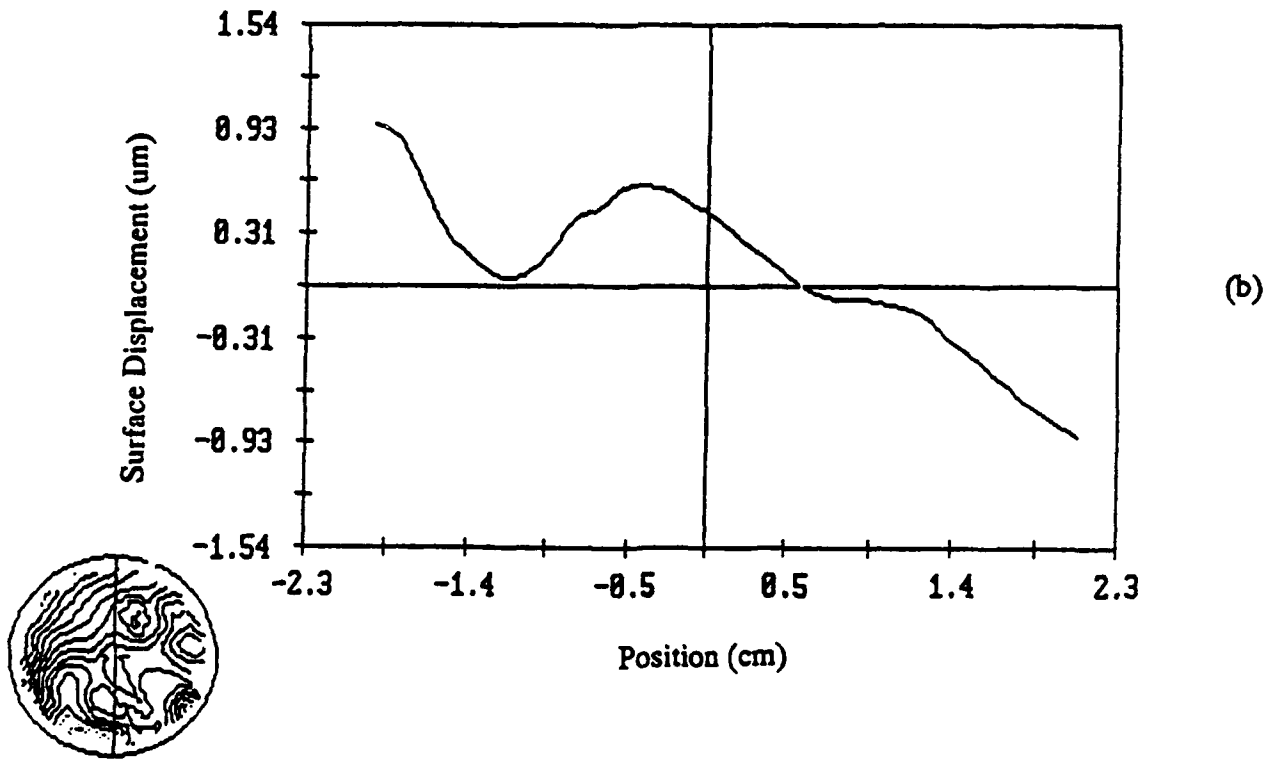
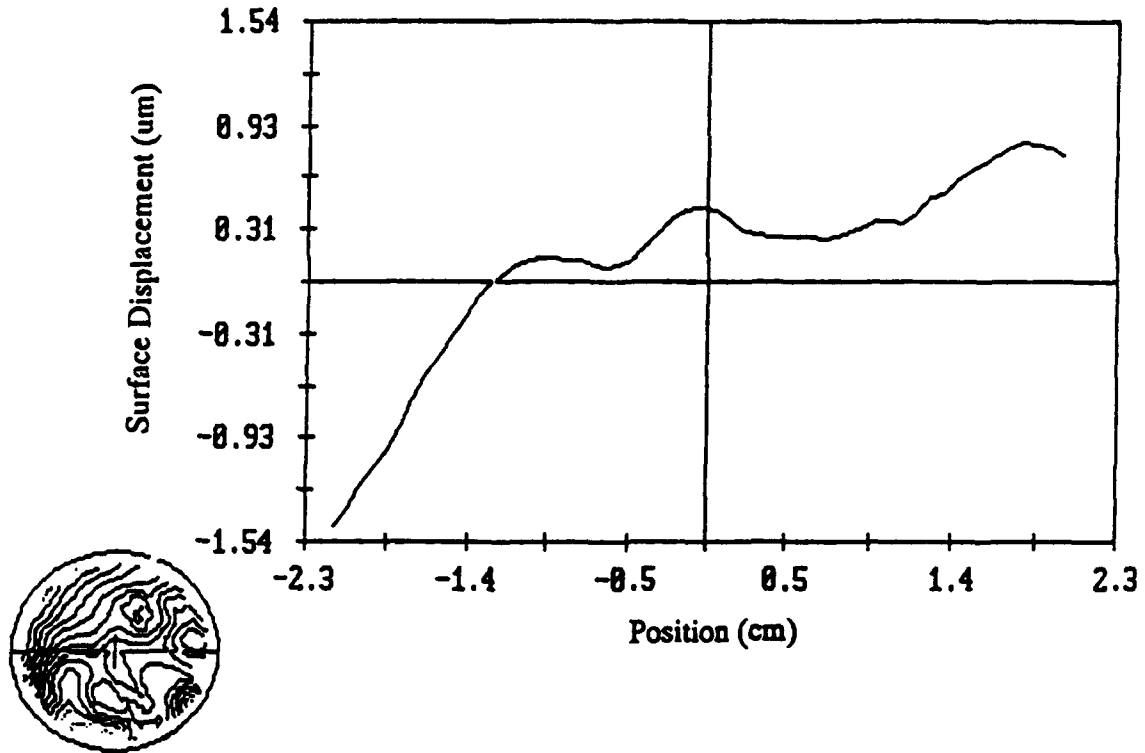


Figure 10.

Typical X-Y profile of the interferogram shown in figure 7:
 (a) X-profile, and (b) Y-profile.



Figure 11. Photographs of the reconstructed interferometric fringes at $Re_1 = 1.04 \times 10^6$.

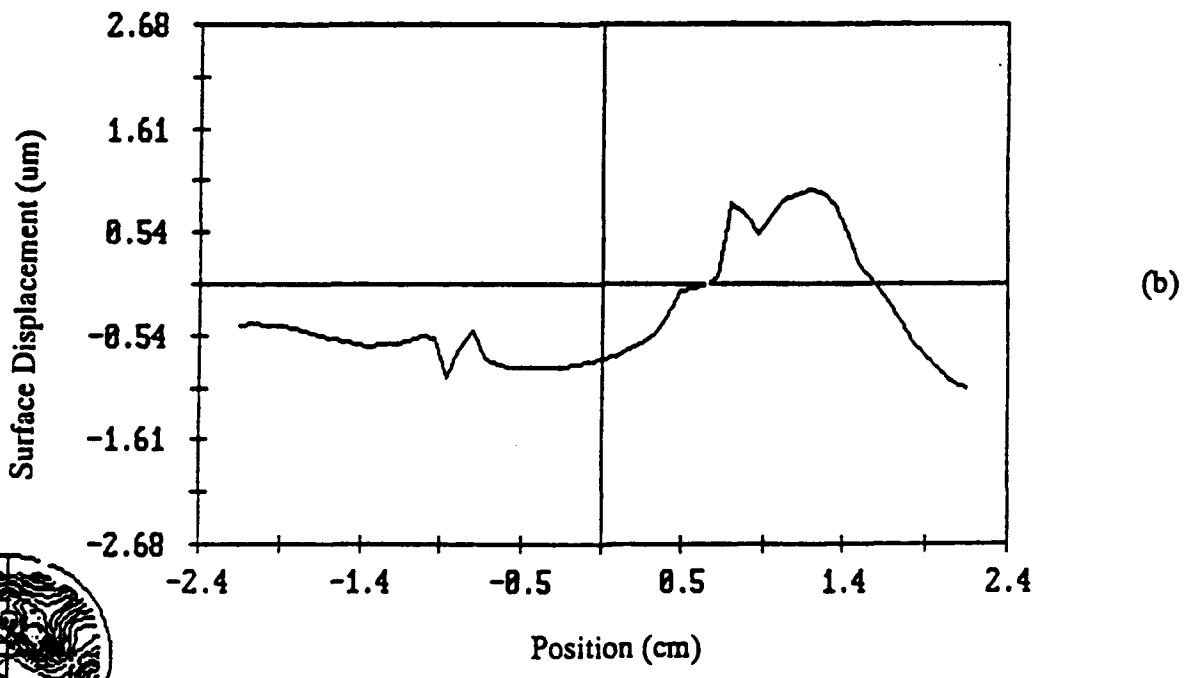
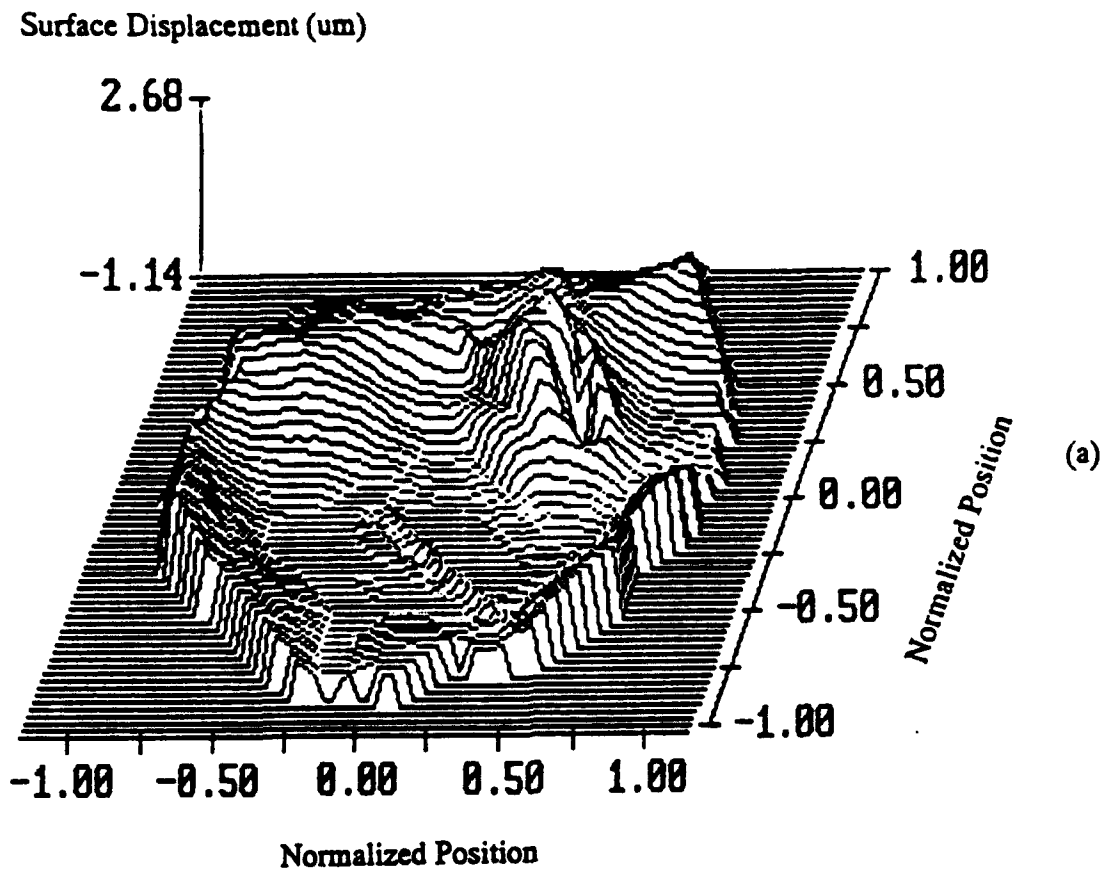


Figure 12. Isometric phase map and the Y-profile of the interferogram shown in figure 11: (a) isometric phase map, and (b) Y-profile.



Figure 13. Photographs of the reconstructed interferometric fringes at $Re_t = 1.43 \times 10^6$.